# Digital adaptive optics line-scanning confocal imaging system

Changgeng Liu
Myung K. Kim

SPIE.

# Digital adaptive optics line-scanning confocal imaging system

Changgeng Liu[†] and Myung K. Kim[*]
University of South Florida, Department of Physics, Digital Holography and Microscopy Laboratory, Tampa, Florida 33620, United States

**Abstract.** A digital adaptive optics line-scanning confocal imaging (DAOLCI) system is proposed by applying digital holographic adaptive optics to a digital form of line-scanning confocal imaging system. In DAOLCI, each line scan is recorded by a digital hologram, which allows access to the complex optical field from one slice of the sample through digital holography. This complex optical field contains both the information of one slice of the sample and the optical aberration of the system, thus allowing us to compensate for the effect of the optical aberration, which can be sensed by a complex guide star hologram. After numerical aberration compensation, the corrected optical fields of a sequence of line scans are stitched into the final corrected confocal image. In DAOLCI, a numerical slit is applied to realize the confocality at the sensor end. The width of this slit can be adjusted to control the image contrast and speckle noise for scattering samples. DAOLCI dispenses with the hardware pieces, such as Shack–Hartmann wavefront sensor and deformable mirror, and the closed-loop feedbacks adopted in the conventional adaptive optics confocal imaging system, thus reducing the opto-mechanical complexity and cost. Numerical simulations and proof-of-principle experiments are presented that demonstrate the feasibility of this idea. © 2015 Society of Photo-Optical Instrumentation Engineers (SPIE) [DOI: 10.1117/1.JBO.20.11.111203]

## 1 Introduction

Adaptive optics (AO) was originally proposed in 1953 by Babcock to compensate for the effect of atmospheric turbulence and improve the resolution of astronomical imaging.[1] The first successful demonstration of a practical AO system was reported in 1977 by Hardy et al.[2] Nowadays, almost all large-scale ground-based telescopes are equipped with AO system to enhance atmospheric imaging.[3,4] To eliminate the effect of ocular aberration and improve the resolution of the retinal image, AO was first incorporated into a wide-field retinal imaging system in 1997 by Liang et al.[5] With the aid of AO, *in vivo* images of the photoreceptors of the human retina are achieved. Since the successful demonstration of AO in wide-field retinal imaging system, different AO systems have been proposed and tested for ophthalmic imaging.[6–10] To improve the image contrast and obtain optical sectioning, AO was incorporated to the point-scanning confocal ophthalmoscope in 2002 by Roorda et al., which enables acquisition of high-contrast retinal images with true optical sectioning capability.[11] A more compact AO confocal retinal imaging system was recently proposed by adopting a line-scanning confocal configuration, which is fundamentally simpler and faster than the point-scanning counterpart.[12–15] AO has also been applied to optical coherence tomography (OCT).[16] However, the application of AO-OCT is still limited by its acquisition speed. A typical AO system contains several critical hardware pieces: a deformable mirror, a lenslet array, and a second CCD camera in addition to the camera for imaging and complicated control of close-loop coordination of the wavefront sensor and wavefront corrector, which limits the translation of AO system from laboratory to clinical use.

To reduce the optomechanical complexity and the cost of the conventional AO system, we have recently introduced a new type of AO system for wide-field retinal imaging based on the principles of digital holography (DH).[17,18] This proposed digital holographic adaptive optics imaging (DHAO) system realizes the aberration sensing and aberration correction by DH and related numerical processing, thus eliminating the need for the hardware pieces such as a Shack–Hartmann wavefront sensor and deformable mirror, and the closed-loop feedbacks imposed by the conventional AO system. The essence of DHAO is to digitally correct the phase aberration by using measured aberration. DHAO is similar to digital adaptive optics systems proposed in Refs. 19 and 20, in which the complex field of the object is obtained by DH and optical aberrations are numerically obtained by using an image metric. Recent work on the computational adaptive optics for interferometric synthetic aperture microscopy has also demonstrated that the numerical correction of the optical aberrations is able to improve the resolution of images from interferometric data.[21] The interferometric data are from a spectral domain OCT system, which is quite different from DH. Different from the work proposed in Refs. 19 and 21, the optical aberrations in DHAO are not from numerical searching but from the direct measurement by DH, thus alleviating the computational burden.

DHAO wide-field imaging is a coherent imaging modality, which suffers from stronger speckle noise for scattering samples, lack of optical sectioning, and lower contrast compared

---

*Address all correspondence to: Myung K. Kim, E-mail: mkkim@usf.edu

†Current Address: Yale School of Medicine, Department of Diagnostic Radiology, New Haven, Connecticut 06520, United States

to the confocal imaging system. In this paper, we apply DHAO to a digital form of a line-scanning confocal imaging system in which each line scan is recorded by a digital hologram.[22] Compared to the digital point-scanning confocal system in which each point scan is recorded by a digital hologram, a digital line-scanning confocal system is three orders of magnitude faster and more tractable in terms of the data flow involved.[23,24] This proposed digital adaptive optics line-scanning confocal imaging (DAOLCI) system is essentially using the amplitude point spread function (PSF) to compensate the amplitude line spread function (LSF). The optical apparatus and the basic principles are presented in Sec. 2. Simulation results are reported in Sec. 3. We then present the experimental demonstration in Sec. 3. Conclusions are drawn in Sec. 4.

## 2 DAOLCI Apparatus and Principle

The optical system of DAOLCI is illustrated in Fig. 1. Because DAOLCI is intended for ophthalmic imaging, the optical system is described by use of a model eye. Figure 1(a) shows the layout of the optical system. A model eye is composed of an eye lens EL with a focal length $f_{EL}$ of 25 mm, and an artificial aberrator



A at the pupil plane and a scattering sample at the focal plane of the eye lens EL. The focal length $f_1$ of the lens L1 is 200 mm, which is put 200 mm away from the eye pupil. The CCD is placed 200 mm away from the lens L1. In the illumination path, a cylindrical lens CL with a focal length $f_{CL}$ of 150 mm is inserted as shown in Fig. 1(a). The details of the illumination configuration are illustrated in Figs. 1(b) and 1(c). Under this illumination, a focal line is projected onto the sample at a time. In this instance, a horizontal line ($x$ direction) is projected on the sample. The sample is mounted on a motorized stage and scanned in the vertical ($y$) direction. The CCD is also put at the conjugate plane of the sample. Because of the aberration added at the pupil, the optical field $O(x_C, y_C, n)$ at the CCD plane from the $n$th scan is distorted, where $(x_C, y_C)$ are the coordinates at the CCD plane. $O(x_C, y_C, n)$ can be related to the field $O(x_P, y_P, n)$ at the pupil by[25]

$$O(x_C, y_C, n) = \frac{1}{j\lambda f_1} \iint O(x_P, y_P, n)$$
$$\times \exp\left[-j2\pi \frac{1}{\lambda f_1}(x_C x_P + y_C y_P)\right] dx_P dy_P, \quad (1)$$

where $\lambda$ is the wavelength of the light source, and $(x_P, y_P)$ are the coordinates at the pupil plane. $O(x_P, y_P, n)$ can be written as

$$O(x_P, y_P, n) = O_U(x_P, y_P, n) P(x_P, y_P) \exp[j\Phi(x_P, y_P)], \quad (2)$$

where $O_U(x_P, y_P, n)$ denotes the undistorted field at the pupil from the $n$th scan, $P(x_P, y_P)$ means the ideal pupil function, and $\Phi(x_P, y_P)$ represents the phase aberration introduced by the aberrator A. Ignoring the prefactor, Eq. (1) can be rewritten as

$$O(f_x, f_y, n) = FT\{O(x_P, y_P, n)\}(f_x, f_y), \quad (3)$$

where

$$f_x = \frac{x_p}{\lambda f_1} \qquad f_y = \frac{y_p}{\lambda f_1}. \quad (4)$$

The optical field $O(x_C, y_C, n)$ can be obtained by off-axis DH, which is realized by introducing a reference beam after collimator C3 in Fig. 1(a) at an angle with respect to the object field.[26–28] The distorted confocal intensity from $n$th scan can be expressed as

$$I_{Conf}(x_C, n) = \sum_{y_C \in slit} |O(x_C, y_C, n)|^2, \quad (5)$$

where the slit means the applied numerical slit. To correct the confocal image, we must measure the aberration $\Phi(x_P, y_P)$ and remove it from Eq. (2). To measure this aberration $\Phi(x_P, y_P)$, a narrow beam is sent into the eye lens EL to generate a guide star at the sample S, which is realized by an inverted telescope system consisting of the lens L2 and L3, as shown in Fig. 1(a). The light scattered from the sample experiences the aberration $\Phi(x_P, y_P)$ introduced by the aberrator A at the pupil plane. A collimated beam through the beam collimator C3 is used as the reference beam so that a guide star hologram can be formed at the CCD. From this guide star hologram, one can retrieve the amplitude PSF of this optical system, as follows:
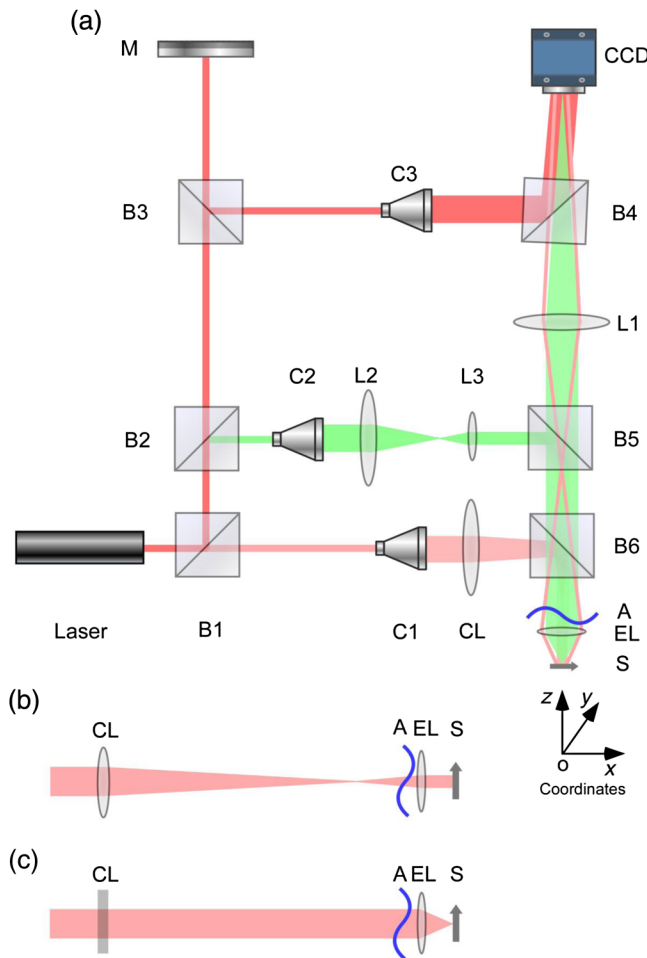
**Fig. 1** Schematic diagram of the optical system of digital adaptive optics line-scanning confocal imaging. (a) Top view of the optical apparatus. BS1 to BS6, beamsplitters; C1 to C2, beam collimators; L1 to L3, lens; CL, cylindrical lens; A, aberrator; EL, eye lens; S, sample; M, mirror. (b) Top view of the line-shaped illumination configuration (in x-z plane). (c) Side view of the line-shaped illumination configuration (in y-z plane).
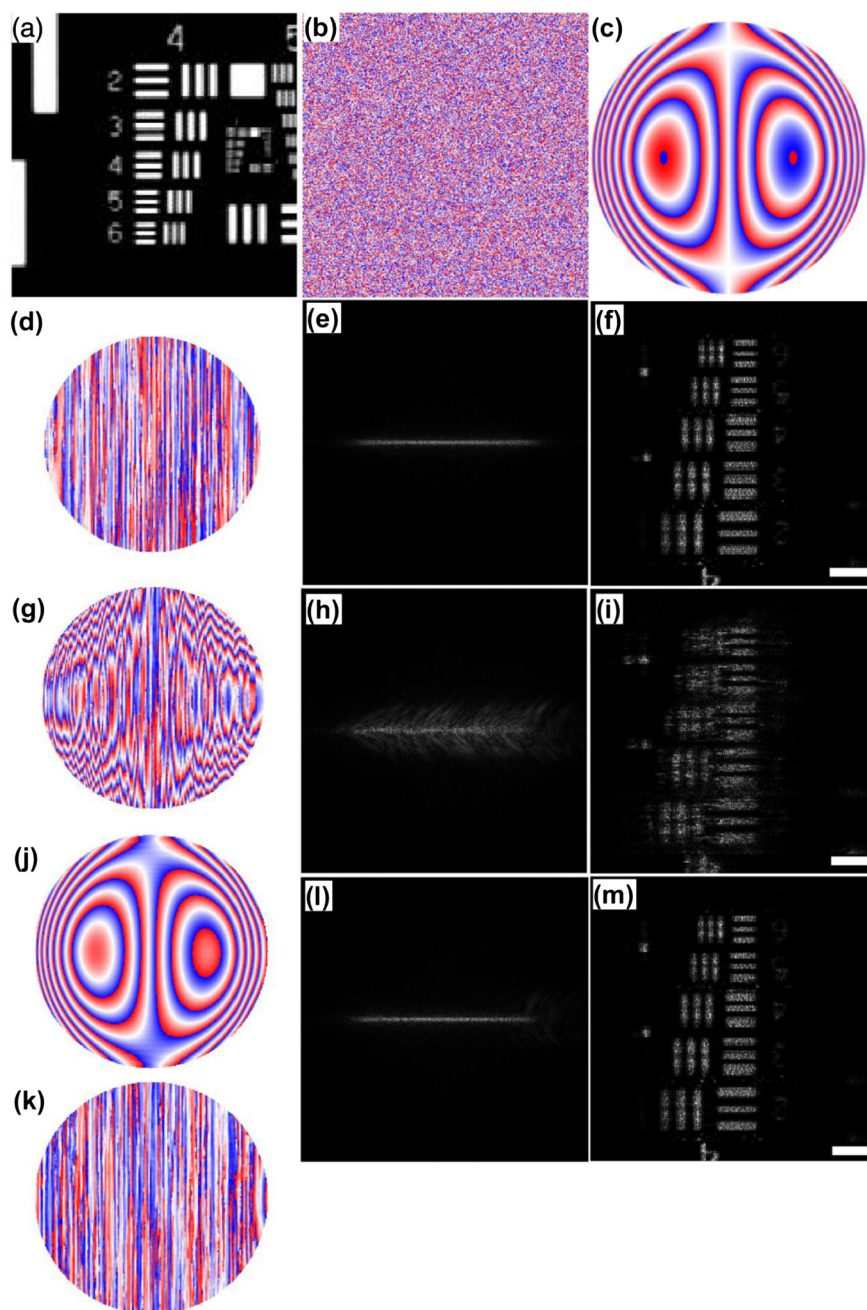
**Fig. 2** Simulation results: (a) and (b) simulated amplitude and phase, (c) phase aberration, (d) phase of optical field at the pupil from one scan without aberration, (e) single line image without aberration, (f) confocal image without aberration, (g) phase of the aberrated optical field at the pupil, (h) distorted line image, (i) distorted confocal image, (j) measured aberration, (k) phase of the corrected field at the pupil, (l) recovered line image, and (m) recovered confocal image. Scale bars: 100 $\mu$m.

$$PSF(f_x, f_y) = FT\{P(x_P, y_P)\exp[j\Phi(x_P, y_P)]\}(f_x, f_y), \tag{6}$$

where the spatial frequency coodinates $(f_x, f_y)$ are related to spatial coodinates $(x_P, y_P)$ at the pupil plane by Eq. (4). Taking the inverse Fourier transform (FT) of Eq. (6), the aberration $\Phi(x_P, y_P)$ within the pupil can be obtained. Within aberration in hand, we are able to correct the aberrated field from each scan. Specifically, taking the inverse FT of $O(x_C, y_C, n)$ to obtain the aberrated field at the pupil $O(x_P, y_P, n)$ and removing the phase aberration from it by $O(x_P, y_P, n)\exp[-j\Phi(x_P, y_P)]$,

we can recover the optical field $O_U(x_P, y_P, n)$ within the pupil. The corrected field $O_C(x_C, y_C, n)$ at the CCD plane is then obtained by taking the FT of this recovered object field $O_U(x_P, y_P, n)$. The final corrected confocal image becomes

$$I_{\text{Conf}}^C(x_C, n) = \sum_{y_C \in \text{slit}} |O_C(x_C, y_C, n)|^2. \tag{7}$$

DAOLCI treats the optical field from each scan as the DHAO wide-field imaging system does for the optical field of the whole object.[18] The selective illumination and numerical slit ensures
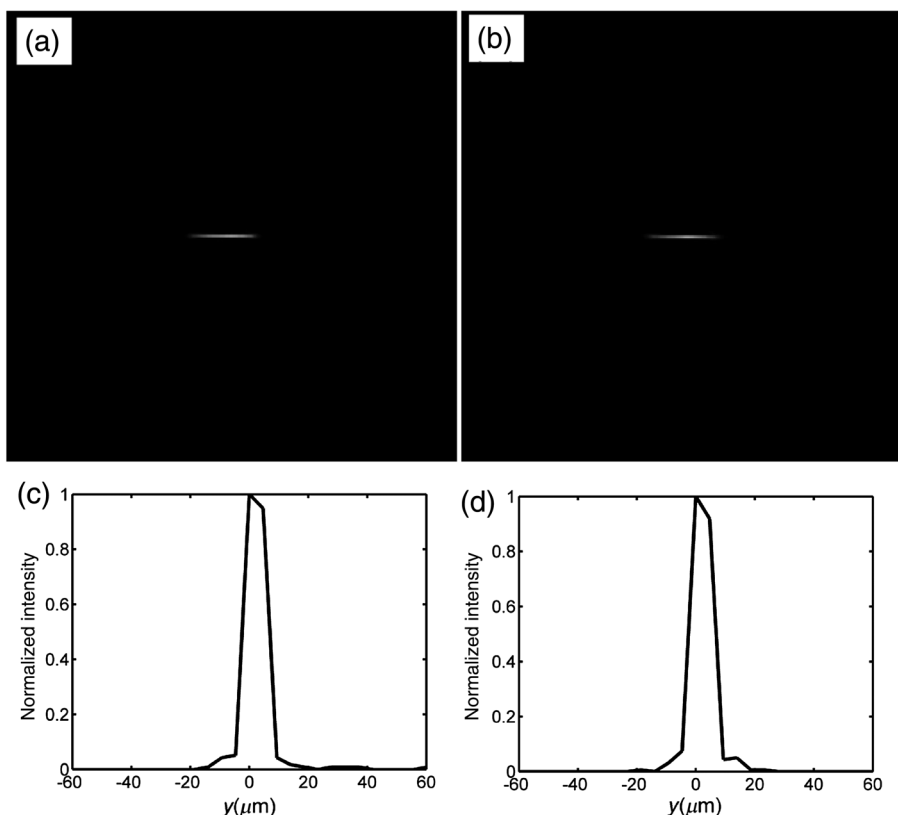
**Fig. 3** Intensities of the focal lines at the sample plane in the experiment: (a) focal line without aberration, (b) focal line with aberration, (c) profile in the vertical direction of (a), and (d) profile in the vertical direction of (b).

the confocality of DAOCLI, which can reject the scattering from the out-of-focus plane and improve the image contrast.

## 3 Simulations

To demonstrate the validity of DAOLCI, we first present a simulation example. In the computer simulation, the radiation wavelength is set to be 632.8 nm. We set the beam size on the cylindrical lens CL as 3 mm to avoid distortion of the illumination on the sample. The scanning step is set to be 3 $\mu$m. The diameter of the pupil is 5 mm. The focal length $f_{CL}$ of the cylindrical lens CL is set to be 150 mm. The imaging numerical aperture is ~0.1, and the corresponding diffraction limited resolution element is ~3.9 $\mu$m. The width of numerical slit to be applied is 9 pixels, which corresponds to one diffraction-limited resolution element.[22] The amplitude of the sample we used is part of a digital resolution target, and the phase of the sample is an array of random phase ranging from $-\pi$ to $+\pi$. Figures 2(a) and 2(b) show the amplitude and phase of this sample. The phase is displayed by a red–white–blue color map throughout this paper. The simulated aberration, as shown in Fig. 2(c), is added at the pupil plane of the lens EL. This aberration is generated by the Zernike polynomials $\Phi = 8\pi(3r^3 - 2r)\sin(\theta)$, where $(r, \theta)$ is the normalized polar coordinate at the pupil. As a baseline, the phase distribution at the pupil without aberration is shown in Fig. 2(d), and the corresponding line image that is the intensity of one scan obtained by taking the FT of the optical field at the pupil plane represented by Fig. 2(d) and the confocal image are shown in Figs. 2(e) and 2(f), respectively. The length of the line image in Fig. 2(e) is ~428 $\mu$m, which determines the width of the confocal image shown in Fig. 2(f). The height of the confocal image is determined as

the product of the number of line scans and the scanning step, which is 768 $\mu$m. The distorted phase distribution at the eye pupil due to the added aberration is shown in Fig. 2(g). The distorted line image as shown in Fig. 2(h) is highly widened compared to the undistorted one as shown in Fig. 2(e). The resulting distorted confocal image, as shown in Fig. 2(i), is significantly blurred by the aberration. To restore the distorted images, aberration is measured by a guide star hologram, as shown in Fig. 2(j). Subtracting this measured aberration from the distorted field at the eye pupil in Fig. 2(g), the corrected field is shown in Fig. 2(k). Taking the FT of this corrected field, the corrected line image can be obtained as shown in Fig. 2(l), which is completely restored. The restored confocal image is shown in Fig. 2(m), which shows pronounced improvement in terms of resolution and contrast compared to the distorted one in Fig. 2(i), thus demonstrating the effectiveness of DHAO for line-scanning confocal imaging system.

## 4 Experimental Results and Discussion

In this section, we present experiments to further validate the feasibility of DAOLCI. In the experiment, a He–Ne laser of wavelength 632.8 nm is the light source. The scattering sample is made by tightly attaching a piece of Teflon tape behind a positive 1951 United States Air Force resolution target and tilting to remove the specular reflections from the surfaces of the resolution target. A piece of broken glass is inserted at the pupil plane, serving as the aberrator A. The pupil size is set to be 5 mm in diameter. Group 4 elements 4 to 5 of the resolution target are imaged. A CCD of $1024 \times 768$ square pixels with a 4.65 $\mu$m pitch is used, of which $512 \times 512$ pixels are employed as the
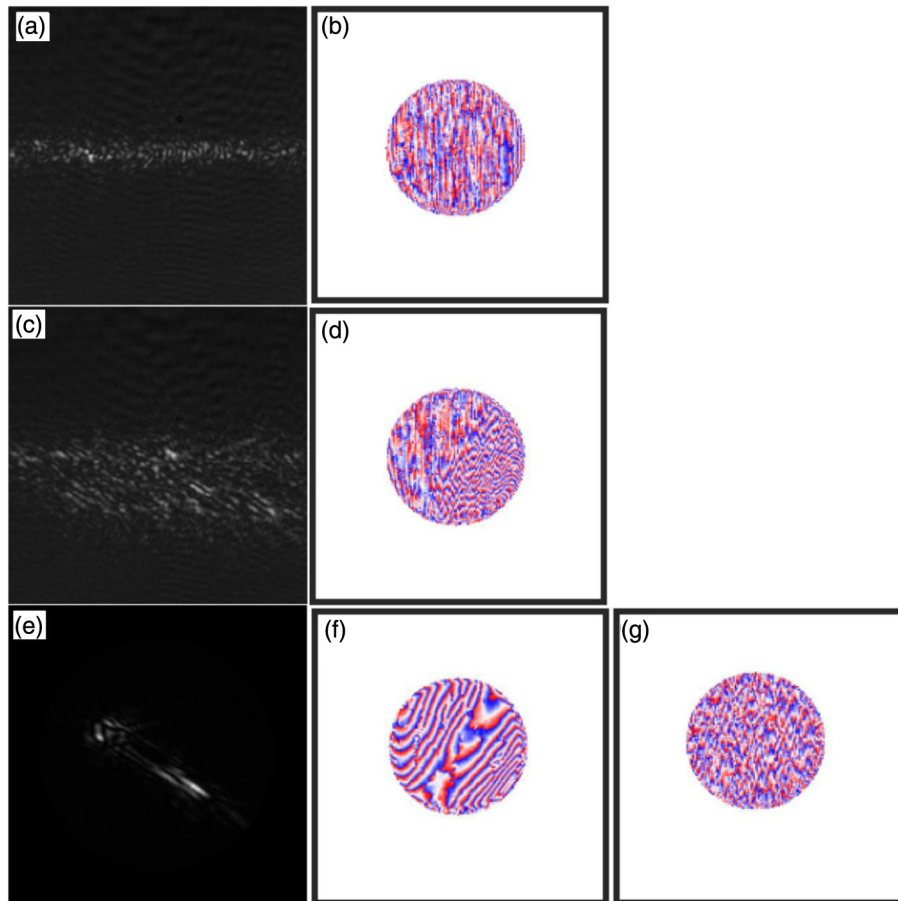
**Fig. 4** Holograms and phase distributions at the eye pupil from the experiment: (a) aberration-free line hologram, (b) aberration-free phase at the pupil plane, (c) distorted line hologram, (d) distorted phase at the pupil plane, (e) guide star hologram, (f) measured aberration from (e), and (g) corrected phase at the pupil plane.

active detection region. The calibrated magnification of the image at the CCD to the object at the sample plane is 8.6, which means the pixel resolution of the confocal image along nonscanning direction is 0.54 $\mu$m. The scanning speed is set to be 10.8 $\mu$m/s such that the pixel resolutions along the scanning and nonscanning directions are the same. A total of 512 scans are taken for the confocal image. The time taken for one full-field image is ∼25.6 s. The field of view of the confocal images is therefore $276 \times 276 \ \mu$m$^2$. The beam illuminating the cylindrical lens CL is set to be ∼2.5 mm in diameter to avoid the distortion of the focal line illumination at the sample. To verify that the effect of aberration on the illumination is negligible with this narrow beam, we put a second CCD at the focal plane of the eye lens EL. The intensities of the focal lines, obtained without and with the aberrator in place, are shown in Figs. 3(a) and 3(b), respectively. Their profiles along the vertical ($y$) directions through the centers of the images are shown in Figs. 3(c) and 3(d). The full-width at half-maximum of these two profiles are both ∼9.4 $\mu$m, indicating that the effect of the aberration on the line focuses can be ignored. The blurring effect on the imaging will be solely from the second passage through the aberrator.

Figure 4(a) shows the hologram of the optical field from one slice of the sample without the aberrator in place. Figure 4(b) shows the phase distribution at the pupil plane, which is obtained by taking inverse FT of the hologram [Fig. 4(a)]

and numerical filtering. The detailed procedures of obtaining the phase at the pupil plane from the hologram can be found in Ref. 18.

The distorted line hologram due to the aberrator is shown in Fig. 4(c). The corresponding distorted phase at the pupil is shown in Fig. 4(d). To measure the aberration, a narrow beam ∼2 mm in diameter is sent through the eye lens EL to generate the guide star at the sample. The reason that we limit the size of the beam for guide star generation is that the aberration will severely blur the focused spot at the sample if we apply a large beam.

The resulting guide star hologram is shown in Fig. 4(e). The phase aberration obtained from this guide star hologram is shown in Fig. 4(f). Figure 4(g) shows the corrected phase distribution at the pupil plane by subtracting Fig. 4(f) from Fig. 4(d). The resultant line and confocal images are shown in Fig. 5. Figure 5(a) shows the line image that is the intensity of one scan obtained by taking FT of the undistorted optical field at the pupil plane represented by Fig. 4(b), serving as a baseline. Figure 5(b) shows the undistorted confocal image where a numerical slit of 21 pixels is applied. This width corresponds to approximately three times the diffraction-limited resolution element. For strongly scattering samples, as used in this experiment, a slightly wide numerical slit can reduce the speckle noise without sacrificing the contrast and resolution. If we apply a much wider slit, the speckle noise can be further reduced, but
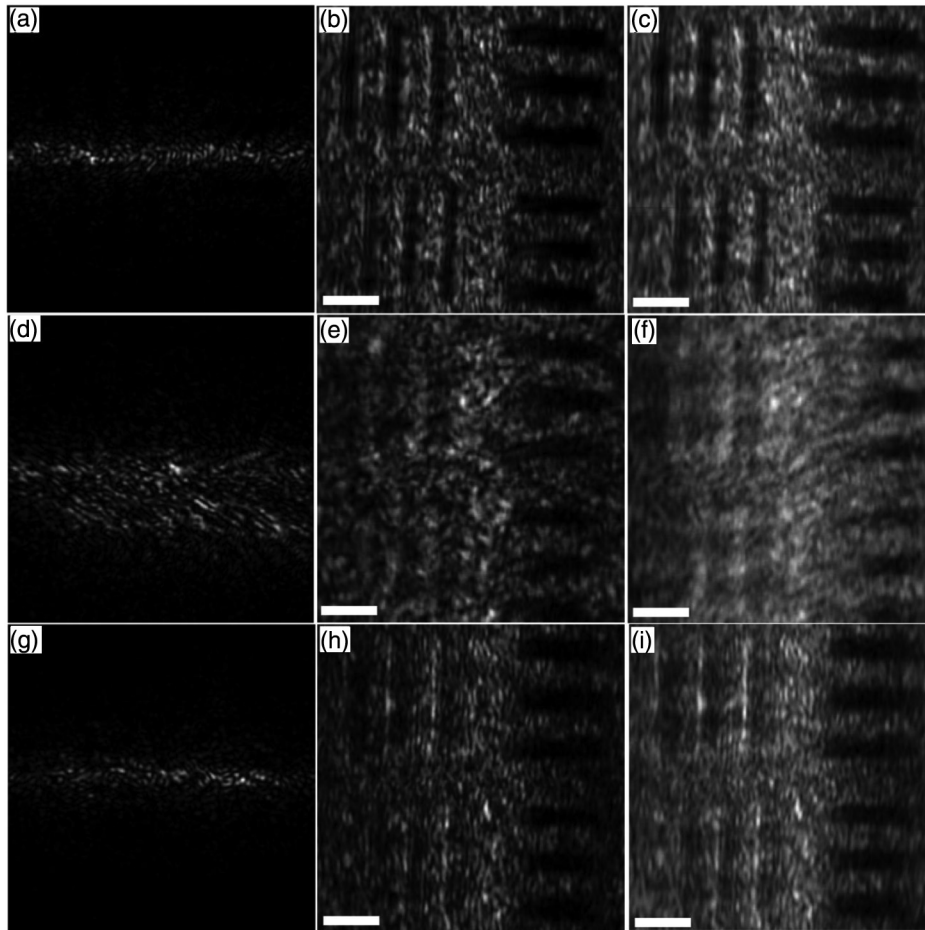
**Fig. 5** Line and confocal images from the experiment: (a) line image without added aberration, (b) confocal image without aberration; the slit width is 21 pixels, (c) confocal image without aberration; the slit width is 210 pixels, (d) distorted line image, (e) distorted confocal image with a slit width of 21 pixels, (f) distorted confocal image with a slit width of 210 pixels, (g) recovered line image, (h) recovered confocal image with a slit width of 21 pixels, and (i) recovered confocal image with a slit width of 21 pixels. Scale bars: 50 $\mu$m.

a significant reduction in contrast will be incurred, as shown in Fig. 5(c), with a slit width of 210 pixels. Also, the optical sectioning capability will be compromised. The optical sectioning capability of the digital line-scanning confocal system arises from the selective illumination and numerical slit at the detection. This is the same as a conventional confocal system.[22] The optical sectioning capability will be reduced as the slit or pinhole is enlarged.[29] The observation on the effect of the size of slit on the speckle contrast agrees well with the work of a point-scanning confocal system.[30]

The distorted line image, as shown in Fig. 5(d), is obtained by taking FT of the distorted optical field at the pupil plane represented by Fig. 4(d). The aberration significantly widens the line image. The resultant confocal image with a slit width of 21 pixels is shown in Fig. 5(e). This confocal image is the best from visual observation while we move the center of numerical slit through the blurred line image. Increase in the slit width leads to stronger cross-talk due to the directional spread of the energy within the line image, as shown in Fig. 5(f), where the slit width is 210 pixels. The corrected line image obtained by taking the FT of the corrected optical field at the pupil represented by Fig. 4(g) is shown in Fig. 5(g). After correction, the width of the line image is recovered to the level of the aberration-free one as shown in Fig. 5(a). The corrected confocal image with a slit

width of 21 pixels is shown in Fig. 5(h), which illustrates almost complete recovery of the information compared to the distorted confocal image in Fig. 5(e). The confocal image with a slit width of 210 pixels is shown in Fig. 5(i), which shows pronounced improvement compared to Fig. 5(f). This is because correction eliminates the strong cross-talk due to the directional spread of energy within the line image. This experiment clearly demonstrates the feasibility of DAOLCI.

## 5 Conclusions

A digital line-scanning confocal imaging system with AO capability is presented. In DAOLCI, the complex amplitude of each scan is the amplitude LSF of the optical system and the complex guide star hologram records the amplitude PSF. In essence, DAOLCI realizes the compensation for the amplitude LSF by use of the amplitude PSF. For an aberration-free imaging system, the information is concentrated within a compact LSF. Aberration spreads this compact LSF in a manner that depends on the type and strength of the aberration. DHAO functions as a mechanism for the readjustment of this widened distribution back into a compact one within the LSF. Simulations and experiments have demonstrated the validity of this idea. Different from our previous work on DHAO, which is a full-field imaging modality,[17,18] DAOLCI is a confocal imaging technique that can achieve

higher-contrast images and optical sectioning. Our line-scanning confocal imaging system has proved to be an effective imaging tool for weakly scattering objects such as retina using spatially coherent light sources, such as diode lasers or superluminescent diodes.[12,31] Although in the demonstration we adopt a He–Ne laser as our light source to simplify the optical system, DAOLCI can be directly applied to diode laser or superluminescent diode by use of low-coherence DH.[32–36] Compared to the classical AO confocal imaging modality, DAOLCI does not require certain hardware pieces, such as a Shack–Hartmann wavefront sensor, deformable mirror, and He closed-loop feedbacks, and also opens the possibilities of adopting computational AO techniques[19–21] to correct for the aberration. As all the conventional AO ophthalmoscopes adopt, we have assumed the aberration happens at or close to the pupil. If the aberration exists in the volume inside the eye, the presented imaging system may integrate some computational methods as reported in Refs. 37 and 38 to deal with this problem. To achieve real-time imaging, beam scanning with a high-speed area camera will become necessary because the optical field from each scan has to be recorded in a two-dimensional frame to retain the aberration of the optical system. If the aberration is not very severe, the requirement of the recording area may be reduced to improve the speed.

## Acknowledgments

## References

1. H. W. Babcock, "The possibility of compensating astronomical seeing," *Publ. Astron. Soc. Pac.* **65**, 229–236 (1953).
2. J. W. Hardy, J. E. Lefebvre, and C. L. Koliopoulos, "Real-time atmospheric compensation," *J. Opt. Soc. Am.* **67**, 360–369 (1977).
3. M. A. van Dam, D. L. Mignant, and B. A. Macintosh, "Performance of the Keck observatory adaptive optics system," *Appl. Opt.* **43**, 5458–5467 (2004).
4. M. Hart, "Recent advances in astronomical adaptive optics," *Appl. Opt.* **49**, D17–D29 (2010).
5. J. Liang, D. R. Williams, and D. Miller, "Supernormal vision and high-resolution retinal imaging through adaptive optics," *J. Opt. Soc. Am. A* **14**, 2884–2892 (1997).
6. K. M. Hampson, "Adaptive optics and vision," *J. Mod. Opt.* **55**, 3425–3467 (2008).
7. I. Iglesias et al., "Extended source pyramid wave-front sensor for the human eye," *Opt. Express* **10**, 419–428 (2002).
8. N. Doble et al., "Use of a microelectromechanical mirror for adaptive optics in the human eye," *Opt. Lett.* **27**, 1537–1539 (2002).
9. S. R. Chamot, C. Dainty, and S. Esposito, "Adaptive optics for ophthalmic applications using a pyramid wavefront sensor," *Opt. Express* **14**, 518–526 (2006).
10. Q. Mu et al., "Liquid crystal based adaptive optics system to compensate both low and high order aberrations in a model eye," *Opt. Express* **15**, 1946–1953 (2007).
11. A. Roorda et al., "Adaptive optics scanning laser ophthalmoscopy," *Opt. Express* **10**, 405–412 (2002).
12. M. Mujat et al., "Compact adaptive optics ophthalmoscope," *Opt. Express* **17**, 10242–10258 (2009).
13. K. Im et al., "Simple high-speed confocal line-scanning microscope," *Opt. Express.* **13**, 5151–5156 (2005).
14. D. X. Hammer et al., "Line-scanning laser ophthalmoscope," *J. Biomed. Opt.* **11**, 041126 (2006).
15. P. J. Dwyer, C. A. Dimarzlo, and M. Rajadhyaksha, "Confocal theta line-scanning microscope for imaging human tissues," *Appl. Opt.* **46**, 1843–1851 (2007).
16. R. J. Zawadzki et al., "Untrahigh-resolution optical coherence tomography with monochromatic and chromatic aberration correction," *Opt. Express* **16**, 8126–8143 (2008).
17. C. Liu and M. K. Kim, "Digital holographic adaptive optics for ocular imaging: proof of principle," *Opt. Lett.* **36**, 2710–2712 (2011).
18. C. Liu, X. Yu, and M. K. Kim, "Fourier transform digital holographic adaptive optics imaging system," *Appl. Opt.* **51**, 8449–8454 (2012).
19. J. Fienup and J. J. Miller, "Aberration correction by maximizing generalized sharpness metrics," *J. Opt. Soc. Am.* **A20**, 609–620 (2003).
20. S. T. Thurman and J. Fienup, "Phase-error correction in digital holography," *J. Opt. Soc. Am. A* **25**, 983–994 (2008).
21. S. G. Adie et al., "Computational adaptive optics for broadband optical inteferometric tomography of biological tissue," *PNAS* **109**, 7175–7180 (2012).
22. C. Liu, S. Marchesini, and M. K. Kim, "Quantitative phase-contrast confocal microscope," *Opt. Express* **22**, 17830–17839 (2014).
23. A. S. Goy and D. Psaltis, "Digital confocal microscope," *Opt. Express* **20**, 22720–22727 (2012).
24. A. S. Goy, M. Unser, and D. Psaltis, "Multiple contrast metrics from the measurements of a digital confocal microscope," *Biomed. Opt. Express* **4**, 1091–1103 (2013).
25. J. Goodman, *Introduction to Fourier Optics*, 3rd ed, pp. 105–107, Roberts and Company Publishers, New York (2005).
26. U. Schnars and W. Jüptner, "Direct recording of holograms by a CCD target and numerical reconstruction," *Appl. Opt.* **33**, 179–181 (1994).
27. E. Cuche, P. Marquet, and C. Depeursinge, "Digital holography for quantitative phase-contrast Imaging," *Opt. Lett.* **24**, 291–293 (1999).
28. M. K. Kim, *Digital Holographic Microscopy: Principles, Techniques, and Applications*, pp. 55–93, Springer, New York (2011).
29. J. B. Pawley, Ed., *Handbook of Biological Confocal Microscopy*, pp. 113–126, Plenum Press, New York (1990).
30. C. Glazowski and M. Rajadhyaksha, "Optimal detection pinhole for lowering speckle noise while maintaining adequate optical sectioning in confocal reflectance microscopes," *J. Biomed. Opt.* **17**, 085001 (2012).
31. Q. Zhang et al., "In vivo confocal imaging of fast intrinsic optical signals correlated with frog retinal activation," *Opt. Lett.* **36**, 4692–4694 (2011).
32. F. Dubois, L. Joannes, and J. C. Legros, "Improved three-dimensional imaging with digital holography microscope with a source of partial spatial coherence," *Appl. Opt.* **38**, 7085–7094 (1999).
33. G. Pedrini and H. J. Tiziani, "Short-coherence digital microscopy by use of lensless holographic imaging system," *Appl. Opt.* **41**, 4489–4496 (2002).
34. F. Dubois and C. Yourassowsky, "Full off-axis red-green-blue digital holographic microscope with LED illumination," *Opt. Lett.* **37**, 2190–2192 (2012).
35. R. Kelner and J. Rosen, "Spatially incoherent single channel digital Fourier holography," *Opt. Lett.* **37**, 3723–3725 (2012).
36. M. K. Kim, "Adaptive optics by incoherent digital holography," *Opt. Lett.* **37**, 2694–2696 (2012).
37. A. E. Tippie and J. Fienup, "Phase-error correction for multiple planes using a sharpness metric," *Opt. Lett.* **34**, 701–703 (2009).
38. A. E. Tippie and J. Fienup, "Multiple-plane anisoplanatic phase correction in a laboratory digital holography experiment," *Opt. Lett.* **35**, 3291–3293 (2010).

**Changgeng Liu** obtained his MS degree in physics in 2010 from Beijing University of Technology. He obtained his PhD degree in applied physics from the University of South Florida in 2015. He is currently a postdoctoral associate at Yale School of Medicine. His research interests include biomedical optics, digital holography, adaptive optics, ophthalmic imaging, and interferometric confocal microscopy.

**Myung K. Kim** is a professor of physics at the University of South Florida and directs the Digital Holography and Microscopy Laboratory. He received his PhD degree from the University of California, Berkeley, in 1986. His current research interests are in the development of novel techniques and applications in digital holography, microscopy, interference imaging, optical tomography, biomedical imaging, and manipulation of particles and microbes by optical force.